Role of anchoring energy on the texture of cholesteric droplets: Finite-element simulations and experiments

Guilhem Poy,* Felix Bunel, and Patrick Oswald
Univ Lyon, Ens de Lyon, Univ Claude Bernard, CNRS, Laboratoire de Physique, F-69342 Lyon, France
(Received 15 May 2017; published 19 July 2017)

We present a numerical method to compute defect-free textures inside cholesteric domains of arbitrary shape. This method has two interesting properties, namely a robust and fast quadratic convergence to a local minimum of the Frank free energy, thanks to a trust region strategy. We apply this algorithm to study the texture of cholesteric droplets in coexistence with their isotropic liquid in two cases: when the anchoring is planar and when it is tilted. In the first case, we show how to determine the anchoring energy at the cholesteric-isotropic interface from a study of the optical properties of droplets of different sizes oriented with an electric field. This method is applied to the case of the liquid crystal CCN-37. In the second case, we come back to the issue of the textural transition as a function of the droplet radius between the double-twist droplets and the banded droplets, observed for instance in cyanobiphenyl liquid crystals. We show that, even if this transition is dominated by the saddle-splay Gauss constant K_4, as was recently recognized by Yoshioka *et al.* [Soft Matter **12**, 2400 (2016)], the anchoring energy does also play an important role that cannot be neglected.

DOI: 10.1103/PhysRevE.96.012705

I. INTRODUCTION

In a free cholesteric phase, the director $\vec{n}$ rotates around a single space direction by forming the so-called equilibrium cholesteric helix. When the cholesteric phase is confined, for instance inside a droplet, the helix is deformed due to the anchoring conditions on the droplet surface. If the anchoring is sliding in the plane of the surface, which we assume in this paper, the anchoring potential γ only depends on the angle θ between the director and the normal to the surface $\vec{\nu}$ and passes through a minimum for a preferred angle θ_a with $\gamma(\theta) \sim W_a(\theta - \theta_a)^2$ at small deviations $|\theta - \theta_a| \ll 1$. Angle θ_a is called the anchoring angle and W_a is the anchoring energy.

Previous studies [1–7] have shown that the texture of a cholesteric droplet (defined by its internal vector field $\vec{n}$) can be extremely various. Let K be a typical Frank constant. Two limit cases can be defined depending on the strength of the anchoring: the *strong anchoring* regime when the extrapolation length $l_a = K/W_a$ is typically less than $0.1\,\mu$m and the *moderate and weak* anchoring regime when $l_a > 0.1\,\mu$m.

In the first regime (strong anchoring), the topological constraints on the surface of the droplet usually induce a frustration of the chiral ordering and the formation of topological defects [1]. This regime is relevant in suspensions of liquid crystal (LC) dispersed in an isotropic fluid such as water [2] or in a polymer matrix (PDLC or polymer-dispersed liquid crystal) [3]. This regime is theoretically interesting because it allows the testing of fundamental topological properties in frustrated systems and the characterization of complex metastable structures [4]. This regime is also technologically interesting, in particular in the field of the LC displays and of the photonic devices: in these applications, electric field and/or lasers can be used to manipulate the internal texture of the droplet and modify its optical properties [5].

In the second regime (moderate and weak anchoring), the topological constraints are generally not strong enough to stabilize the defects in the bulk of the droplet, which leads to more simple structures. This regime is relevant in cholesteric droplets in thermodynamic coexistence with the isotropic phase of the same LC, because the surface tension, and thus the anchoring energy, is much smaller than in the previous LC suspensions and PDLCs. Experimentally, the textures inside such droplets were studied by Yoshioka *et al.* [6] and by one of us (P.O.) [7], who, respectively, observed a structural transition between two types of textures in a static case and in a dynamic case.

In principle, the knowledge at each point of the droplet of the full tensorial-order parameter is necessary to completely characterize the texture. This is crucial, in particular when the droplet contains defects. In contrast, knowing the director field is sufficient when there is no defects, because, in this case, the scalar-order parameter can be taken as a constant everywhere. Theoretically, the director field is obtained by minimizing the Frank elastic energy augmented with the appropriate penalization terms (such as the electric energy, the anchoring energy, the Lagrange term accounting for the fact that $\vec{n}$ is a unit vector, etc.). This minimization can rarely be done analytically, and in general, one must rely on experimental and/or numerical methods to reconstruct the director field. For instance, Posnjak *et al.* [2] showed that the director field can be automatically reconstructed by using a fluorescent confocal polarizing microscopy combined with a Monte Carlo algorithm. The main limitation of this method is that the birefringence Δn of the LC must be very small to avoid optical artifacts.

Numerical methods do not suffer from such limitations and are an efficient tool to study the structures inside cholesteric droplets. If the chiral ordering is strongly frustrated (strong anchoring), one must take into account the variation of the order parameter inside the core of the defects and numerically minimize the full Landau–Ginzburg–de Gennes free energy. The minimization is usually done with an Euler relaxation scheme [1,4], which is formally equivalent to a gradient descent algorithm. Alternatively, Bajc *et al.* [8] recently proposed a hybrid method that uses either the Newton method

*guilhem.poy@ens-lyon.fr

 ©2017 American Physical Society

or the gradient descent method when the convergence is difficult.

If there is no defects in the structure—as assumed in this paper—one can take the order parameter constant and only minimize the Frank free energy. Two classes of numerical methods were proposed to minimize the Frank free energy. First, one can use a gradient descent algorithm, as done for instance by Gil *et al.* [9]. But this method, although very robust, presents a slow linear convergence, which can become problematic when studying large 3D domains. Second, a Newton method can be used, as proposed by Adler *et al.* [10] or Gartland *et al.* [11]. This algorithm has a fast quadratic convergence but presents severe limitations: it can converge to any stationary point (including a maximum of the free energy) and can diverge if a singular Hessian is encountered.

In this paper, we present a numerical method to minimize the Frank free energy with a robust quadratic convergence, thus overcoming the limitations of the gradient descent and Newton algorithms.

The plan of the paper is as follows. In Sec. II, we describe our minimization algorithm, based on a finite-element (FE) discretization of the Frank free energy. In Secs. III and IV, we address two problems with this algorithm: the one of the measurement of the anchoring energy at the cholesteric-isotropic interface when the anchoring is planar (Sec. III) and the one of the structural transition between the double-twist droplets and the banded droplets when the anchoring is tilted and the anchoring energy not negligible (Sec. IV). Finally, we draw our conclusions in Sec. V.

II. THE TRUST-REGION ALGORITHM

In this section, we explicit the trust-region algorithm used to find the texture inside cholesteric droplets with finite anchoring energy. This algorithm is based on the renormalized Newton method introduced by Gartland *et al.* [11], with three main differences: the discretization is made on an arbitrary unstructured grid instead of a regular one, a trust-region method is used instead of a Newton method, and an algebraic multigrid preconditioner is used to help the convergence.

A. Continuous optimization problem

First, we recall that the texture inside a droplet corresponds to the unit director field $\vec{n}_s$, which minimizes the free energy:

$$\vec{n}_s = \underset{\vec{n},|\vec{n}|=1}{\operatorname{argmin}} F[\vec{n}], \tag{1}$$

where the free energy $F[\vec{n}] = F_f[\vec{n}] + F_e[\vec{n}] + F_s[\vec{n}]$ is the sum of the Frank energy F_f, the electric energy F_e, and the anchoring energy F_s. The detailed expressions of all contributions are given in Ref. [12]:

$$F_f[\vec{n}] = \int_V \frac{dV}{2}\{K_4|\vec{\vec{\nabla}}\vec{n}|^2 + 2K_2q(\vec{n}\cdot\vec{\nabla}\times\vec{n}) + K_{14}(\vec{\nabla}\cdot\vec{n})^2 + K_{34}(\vec{\nabla}\times\vec{n})^2 + K_{23}(\vec{n}\cdot\vec{\nabla}\times\vec{n})^2\}, \tag{2}$$

$$F_e[\vec{n}] = -\int_V dV\ \frac{\epsilon_0\epsilon_a}{2}(\vec{E}\cdot\vec{n})^2, \tag{3}$$

$$F_s[\vec{n}] = \int_S dS\ \gamma(\vec{n}\cdot\vec{\nu}), \tag{4}$$

where $K_{ij} = K_i - K_j, [\vec{\vec{\nabla}}\vec{n}]_{ij} = n_{j,i}, |\vec{\vec{\nabla}}\vec{n}|^2 = n_{j,i}\,n_{j,i}$, the K_i are the Frank elastic constants, q is the equilibrium twist, ϵ_a is the anisotropy of the dielectric constant, $\vec{E}$ is the electric field, and γ is the anchoring potential of the cholesteric-isotropic interface. Note that in the one-constant approximation $K_i = K$, only the K_2q and K_4 terms in $F_f[\vec{n}]$ are nonzero. In addition, the K_i must obey the Ericksen inequalities [13]:

$$K_i \geqslant 0, \quad K_4 \leqslant \min(2K_2, 2K_1). \tag{5}$$

Due to the symmetries of both the isotropic and cholesteric phases, the anchoring potential can be expressed as an even function of $\vec{n}\cdot\vec{\nu}$, where $\vec{\nu}$ is the normal to the interface:

$$\gamma(\vec{n}\cdot\vec{\nu}) = \begin{cases} W_a(\vec{n}\cdot\vec{\nu})^2 \text{(planar anchoring)}, \\ W_a\left[\frac{(\vec{n}\cdot\vec{\nu})^2 - \cos^2\theta_a}{\sin 2\theta_a}\right]^2 \text{(tilted anchoring)}. \end{cases} \tag{6}$$

In this equation, θ_a is the anchoring angle (with $0 \leqslant \theta_a \leqslant \pi/2$) and W_a is the anchoring energy as defined in the introduction (with $W_a \geqslant 0$).

To account for the constraint $\vec{n}\cdot\vec{n} = 1$, we introduce a pointwise Lagrange multiplier λ and the associated Lagrangian:

$$\mathcal{L}[\vec{n},\lambda] = F[\vec{n}] + \int_V dV\ (\vec{n}\cdot\vec{n} - 1)\lambda. \tag{7}$$

The original problem given in Eq. (1) can therefore be rewritten as the following optimization problem:

$$\delta\mathcal{L}[\vec{n}_s,\lambda_s] = 0, \tag{8}$$

$$\vec{n}_s = \underset{\vec{n}}{\operatorname{argmin}}\ \mathcal{L}[\vec{n},\lambda_s]. \tag{9}$$

This problem is too difficult to be solved analytically, in general. For this reason, we will discretize it using a finite-element space.

B. Discretized optimization problem

Let $\{K_e,\ e = 0...M'-1\}$ be a nondegenerate subdivision of the cholesteric domain V with distorted cubic (or hexahedral) cells and $\{\vec{x}_k,\ k = 0...M-1\}$ the associated vertices. First, we use $\mathcal{Q}_1$ Lagrange elements to approximate $\vec{n}$ and λ:

$$\vec{n}(\vec{x}) = \sum_{i=0}^{3M-1} N_i\ \vec{\phi}_i(\vec{x}), \tag{10}$$

$$\lambda(\vec{x}) = \sum_{\alpha=0}^{M-1} \Lambda_\alpha\ \psi_\alpha(\vec{x}), \tag{11}$$

where the functions $\{\vec{\phi}_i,\psi_i\}$ are piecewise trilinear functions verifying the following relations:

$$\vec{\phi}_i(\vec{x}_k) = \delta_k^{q(i)}\ \vec{e}_{r(i)},$$
$$\psi_\alpha(\vec{x}_k) = \delta_k^\alpha,$$

with $q(i)$ and $r(i)$ the quotient and reminder of the division of i by $\dim(V) = 3$, δ_j^i the Kronecker δ, and $\{\vec{e}_k,\ k = 0...2\}$ an

orthonormal basis for V. Using the last two equations, we can rewrite the vector of nodal director values as

$$\boldsymbol{N} = \begin{bmatrix} \vec{n}_0 \\ \vdots \\ \vec{n}_{M-1} \end{bmatrix}, \tag{12}$$

where $\vec{n}_i \equiv \vec{n}(\vec{x}_i)$.

Second, we approximate all integrals $\int_V \cdot$ (respectively, $\int_S \cdot$) with the associated trapezoidal rule $\langle\cdot\rangle_V$ (respectively, $\langle\cdot\rangle_S$):

$$\langle g\rangle_V \equiv \sum_{e=0}^{M'-1} \sum_{j=0}^{7} \frac{v_e}{8}\, g\big(\vec{x}_{p_v(e,j)}\big), \tag{13}$$

$$\langle g\rangle_S \equiv \sum_{e=0}^{M'-1} \sum_{j=0}^{3} \frac{s_e}{4}\, g\big(\vec{x}_{p_s(e,j)}\big), \tag{14}$$

where v_e is the volume of K_e, s_e is the surface of the boundary face associated with K_e (by convention, $s_e = 0$ if K_e is an interior cell), $p_v(e,j)$ is the global index of the jth vertex on the cell K_e, and $p_s(e,j)$ is the global index of the jth vertex on the boundary face associated with K_e. This choice of integration rule is not exact for the considered finite element space and functional but will allow us to eliminate in a very simple manner the constrained degrees of freedom.

Note that special care must be taken if the integrand in Eqs. (13) and (14) contains gradients of the shape functions $\vec{\phi}_i$ and ψ_α. Indeed, our choice of finite-element space implies that the gradients of these functions are only piecewise continuous and therefore ill-defined on the boundary of each cells. In this case, Eq. (13) [Eq. (14)] must be computed cell by cell (face by face) by replacing each value of the gradient at a vertex with the continuous prolongation of the gradient inside the considered cell (face).

Finally, we use Eqs. (10), (11) and (13), (14) in Eq. (7) to find the discretized Lagrangian $\mathcal{L}_d(\boldsymbol{N},\boldsymbol{\Lambda}) = f(\boldsymbol{N}) + \boldsymbol{C}(\boldsymbol{N})^\intercal\, \boldsymbol{\Lambda}$, with

$$f(\boldsymbol{N}) = \sum_{i,j=0}^{3M-1} \Xi_{ij} N_i N_j + \sum_{i,j,k,l=0}^{3M-1} \Pi_{ijkl} N_i N_j N_k N_l, \tag{15}$$

$$C_\alpha(\boldsymbol{N}) = \sum_{i,j=0}^{3M-1} \langle \psi_\alpha\, \vec{\phi}_i \cdot \vec{\phi}_j\rangle_V N_i N_j - \langle\psi_\alpha\rangle. \tag{16}$$

Detailed expressions for the tensors $\boldsymbol{\Xi}$ and $\boldsymbol{\Pi}$ are not necessary for the following discussion. $\boldsymbol{C}$ can be interpreted as the vector of all pointwise constraints.

We will use the following notation for the Hessian of the Lagrangian, the gradient of the constraint vector, and the gradient of the free energy:

$$\begin{aligned} \boldsymbol{A}(\boldsymbol{N},\boldsymbol{\Lambda}) &= \nabla_{NN}\mathcal{L}_d(\boldsymbol{N},\boldsymbol{\Lambda}), \\ \boldsymbol{B}(\boldsymbol{N}) &= \nabla_N \boldsymbol{C}(\boldsymbol{N}), \\ \boldsymbol{G}(\boldsymbol{N}) &= \nabla_N f(\boldsymbol{N}). \end{aligned}$$

By replacing $\mathcal{L}$ by $\mathcal{L}_d$ in Eqs. (8) and (9), and using Prop. 3.1.1. in the Bertsekas textbook [14], we get the equivalent discrete optimization problem:

$$\boldsymbol{G}(\bar{\boldsymbol{N}}) + \boldsymbol{B}(\bar{\boldsymbol{N}})\ \bar{\boldsymbol{\Lambda}} = 0, \tag{17}$$

$$\boldsymbol{C}(\bar{\boldsymbol{N}}) = 0, \tag{18}$$

$$\forall\, \delta\boldsymbol{N} \in H(\bar{\boldsymbol{N}}), \quad \delta\boldsymbol{N}^\intercal\, [\boldsymbol{A}(\bar{\boldsymbol{N}},\bar{\boldsymbol{\Lambda}})]\, \delta\boldsymbol{N} \geqslant 0, \tag{19}$$

where $H(\bar{\boldsymbol{N}})$ is the subspace of first-order feasible variations:

$$H(\bar{\boldsymbol{N}}) = \{\delta\boldsymbol{N} | \delta\boldsymbol{N}^\intercal\ \boldsymbol{B}(\bar{\boldsymbol{N}}) = \boldsymbol{0}\}.$$

Equation (17) corresponds to the first-order optimality condition, and Eq. (18) is the feasibility condition. Equation (19) shows that the curvature must be positive in all feasible directions at the minimum.

C. Iterative solving

To solve the optimization problem in Eqs. (17)–(19), we will use an iterative procedure. Let $\boldsymbol{N}_{(k)}$ be the solution obtained at the kth iteration. We will assume without loss of generality that this solution verifies the constraint $\boldsymbol{C}(\boldsymbol{N}_{(k)}) = 0$. Indeed, this condition can be easily enforced by using Eq. (12) and the transformation $\vec{n}_i \to \vec{n}_i / |\vec{n}_i|$.

Following Gartland *et al.* [11], we can compute an estimate of the Lagrange multiplier by solving

$$\boldsymbol{\Lambda}_{(k)} = \underset{\boldsymbol{\Lambda}}{\operatorname{argmin}} \|\boldsymbol{G}_{(k)} + \boldsymbol{B}_{(k)}\ \boldsymbol{\Lambda}\|^2,$$

where $\boldsymbol{G}_{(k)} = \boldsymbol{G}(\boldsymbol{N}_{(k)})$ and $\boldsymbol{B}_{(k)} = \boldsymbol{B}(\boldsymbol{N}_{(k)})$. This last equation can be interpreted as the least square solution of the first-order optimality condition in Eq. (17), whose expression is given by

$$\boldsymbol{\Lambda}_{(k)} = -\big[\boldsymbol{B}_{(k)}^\intercal\, \boldsymbol{B}_{(k)}\big]^{-1}\, \boldsymbol{B}_{(k)}\, \boldsymbol{G}_{(k)}. \tag{20}$$

To compute the Lagrange multiplier $\boldsymbol{\Lambda}_{(k)}$, we therefore need the expressions of $\boldsymbol{B}_{(k)}$, $[\boldsymbol{B}_{(k)}^\intercal\, \boldsymbol{B}_{(k)}]^{-1}$, and $\boldsymbol{G}_{(k)}$. The full expression of the matrix $\boldsymbol{B}_{(k)}$, of dimension $3M \times M$, can easily be computed by differentiating Eq. (16):

$$\boldsymbol{B}_{(k)} = \begin{bmatrix} V_0\, \vec{n}_0 & & \\ & \ddots & \\ & & V_{M-1}\, \vec{n}_{M-1} \end{bmatrix}, \tag{21}$$

where $V_\alpha = \sum_{e=0}^{M'-1} \sum_{j=0}^{7} v_e\, \delta_\alpha^{p_v(e,j)}$ is the volume of all the cells containing the vertex $\vec{x}_\alpha$, and the $\vec{n}_\alpha$ are the local values of the director associated with $\boldsymbol{N}_{(k)}$. Due to the very simple structure of $\boldsymbol{B}_{(k)}$, we can directly invert the matrix $\boldsymbol{B}_{(k)}^\intercal\, \boldsymbol{B}_{(k)}$:

$$\big[\boldsymbol{B}_{(k)}^\intercal\, \boldsymbol{B}_{(k)}\big]^{-1} = \begin{bmatrix} 1/V_0^2 & & \\ & \ddots & \\ & & 1/V_{M-1}^2 \end{bmatrix}, \tag{22}$$

where we have used the normalization condition $|\vec{n}_\alpha| = 1$. Finally, the expression of $\boldsymbol{G}_{(k)}$ can be obtained by differentiating Eq. (15):

$$\begin{aligned} [\boldsymbol{G}_{(k)}]_i = {} & \langle K_{14}(\vec{\nabla}\cdot\vec{\phi}_i)(\vec{\nabla}\cdot\vec{n})\rangle_V + \langle [K_2 q + K_{23}(\vec{n}\cdot\vec{\nabla}\times\vec{n})] \\ & (\vec{n}\cdot\vec{\nabla}\times\vec{\phi}_i + \vec{\phi}_i\cdot\vec{\nabla}\times\vec{n})\rangle_V \\ & + \langle K_{34}\,(\vec{\nabla}\times\vec{\phi}_i)\cdot(\vec{\nabla}\times\vec{n})\rangle_V + \langle K_4\,(\overrightarrow{\nabla}\vec{\phi}_i) : (\overrightarrow{\nabla}\vec{n})\rangle_V \\ & - \langle \epsilon_0\epsilon_a\,(\vec{E}\cdot\vec{\phi}_i)(\vec{E}\cdot\vec{n})\rangle_V + \langle \gamma'(\vec{n}\cdot\vec{v})\,\vec{\phi}_i\cdot\vec{v}\rangle_S, \end{aligned} \tag{23}$$

where $\vec{n}$ is the interpolating function associated with $\boldsymbol{N}_{(k)}$ and $\vec{\vec{A}} : \vec{\vec{B}} = \sum_{i,j} A_{ij}\, B_{ij}$.

We now want to find an update $\boldsymbol{\delta N}$, which improves the current solution $\boldsymbol{N}_{(k)}$, i.e., decrease the free energy while keeping the constraints in check:

$$f(\boldsymbol{N}_{(k)} + \boldsymbol{\delta N}) \leqslant f(\boldsymbol{N}_{(k)}),$$
$$\boldsymbol{C}(\boldsymbol{N}_{(k)} + \boldsymbol{\delta N}) = \boldsymbol{0}.$$

For now, let us suppose that the last two conditions are only verified up to order 1 in $\boldsymbol{\delta N}$:

$$\boldsymbol{\delta N}^{\intercal}\, \boldsymbol{G}_{(k)} \leqslant 0, \tag{24}$$

$$\boldsymbol{\delta N}^{\intercal}\, \boldsymbol{B}_{(k)} = \boldsymbol{0}. \tag{25}$$

Equation (25) implies that $\boldsymbol{\delta N}$ is in the null space (or kernel) of the matrix $\boldsymbol{B}_{(k)}$, i.e., there exists a vector $\boldsymbol{\delta N}_{\perp}$ of size $2M$ such that

$$\boldsymbol{\delta N} = \boldsymbol{Z}_{(k)}\, \boldsymbol{\delta N}_{\perp},$$

where $\boldsymbol{Z}_{(k)}$ is a matrix whose column space is the null space of $\boldsymbol{B}_{(k)}$. As in the algorithm of Gartland *et al.* [11], such a matrix is very easy to find due to the simple expression of $\boldsymbol{B}_{(k)}$:

$$\boldsymbol{Z}_{(k)} = \begin{bmatrix} \vec{l}_0 & \vec{m}_0 & & & & \\ & & \vec{l}_1 & \vec{m}_1 & & \\ & & & & \ddots & \\ & & & & \vec{l}_{M-1} & \vec{m}_{M-1} \end{bmatrix}, \tag{26}$$

where the $\vec{l}_i$ and $\vec{m}$ are constructed in order that $\forall i$, $\{\vec{n}_i, \vec{l}_i, \vec{m}_i\}$ is an orthonormal basis. By construction, the matrix $\boldsymbol{Z}_{(k)}$, of dimension $3M \times 2M$, verifies the property $\boldsymbol{Z}_{(k)}^{\intercal}\, \boldsymbol{B}_{(k)} = 0$. In addition, the vector $\boldsymbol{\delta N}_{\perp}$ can be interpreted as the coordinates of the vector $\boldsymbol{\delta N}$ in the local frames $\{\vec{l}_i, \vec{m}_i\}$.

Equation (24) implies that $\boldsymbol{\delta N}$ is a descent direction for the discretized energy f. To find the best possible descent direction, we need to characterize the energy landscape in the neighborhood of $\boldsymbol{N}_{(k)}$. By developing the Lagrangian $\mathcal{L}_d$ up to order 2 in $\boldsymbol{\delta N}$ and using the relation $\boldsymbol{Z}_{(k)}^{\intercal}\, \boldsymbol{B}_{(k)} = 0$, we arrive at the following relation:

$$\mathcal{L}_d(\boldsymbol{N}_{(k)} + \boldsymbol{\delta N}, \boldsymbol{\Lambda}_{(k)}) = m_k(\boldsymbol{\delta N}_{\perp}) + o(\delta N^2),$$

where we have defined

$$m_k(\boldsymbol{\delta N}_{\perp}) = f_{(k)} + \boldsymbol{\delta N}_{\perp}^{\intercal}\, \boldsymbol{G}_{\perp(k)} + \tfrac{1}{2} \boldsymbol{\delta N}_{\perp}^{\intercal}\, \boldsymbol{A}_{\perp(k)}\, \boldsymbol{\delta N}_{\perp},$$
$$f_{(k)} = f(\boldsymbol{N}_{(k)}),$$
$$\boldsymbol{G}_{\perp(k)} = \boldsymbol{Z}_{(k)}^{\intercal}\, \boldsymbol{G}_{(k)}, \tag{27}$$

$$\boldsymbol{A}_{\perp(k)} = \boldsymbol{Z}_{(k)}^{\intercal}\, \boldsymbol{A}_{(k)}\, \boldsymbol{Z}_{(k)}, \tag{28}$$
$$\boldsymbol{A}_{(k)} = \boldsymbol{A}(\boldsymbol{N}_{(k)}, \boldsymbol{\Lambda}_{(k)}).$$

The function m_k represents a quadratic model of the Lagrangian valid only in a certain neighborhood of $\boldsymbol{N}_{(k)}$. Consequently, the best descent direction can be computed from the minimum of m_k on this neighborhood. To estimate the typical size of this neighborhood, we use a trust-region strategy. Let Δ_k be the trust radius associated with the model m_k. A good choice for the descent direction would be to take

$$\boldsymbol{\delta N}_{\perp} = \underset{\boldsymbol{\delta N}_{\perp},\, \|\boldsymbol{\delta N}_{\perp}\| \leqslant \Delta_k}{\operatorname{argmin}} m_k(\boldsymbol{\delta N}_{\perp}). \tag{29}$$

In practice, we approximate the solution of the last equation as the output of the truncated conjugate gradient (TCG) algorithm of Steihaug [15], with an algebraic multigrid (AMG) preconditioner based on the Trilinos ML implementation [16]. The TCG algorithm allows us to find a direction which satisfies the descent condition in Eq. (24) and has two interesting properties: far from (near) the minimum $\bar{\boldsymbol{N}}, \boldsymbol{\delta N}$ will corresponds to the Cauchy (Newton) direction. The first property ensures that the convergence is robust, even when starting far from the minimum, and the second property ensures a quadratic convergence toward $\bar{\boldsymbol{N}}$.

The TCG algorithm requires the values of the reduced gradient $\boldsymbol{G}_{\perp(k)}$ and of the reduced Hessian $\boldsymbol{A}_{\perp(k)}$, which can be assembled from $\boldsymbol{Z}_{(k)}, \boldsymbol{G}_{(k)}$, and $\boldsymbol{A}_{(k)}$. The expressions of $\boldsymbol{G}_{(k)}$ and $\boldsymbol{Z}_{(k)}$ were already given in Eqs. (23) and (26). The expression of $\boldsymbol{A}_{(k)}$ can be obtained by differentiating two times the Lagrangian $\mathcal{L}_d$:

$$\begin{aligned}[\boldsymbol{A}_{(k)}]_{ij} = {} & \langle K_{14}\, (\vec{\nabla} \cdot \vec{\phi}_i)(\vec{\nabla} \cdot \vec{\phi}_j) \rangle_V + \langle [K_2 q + K_{23} (\vec{n} \cdot \vec{\nabla} \times \vec{n})]\, (\vec{\phi}_j \cdot \vec{\nabla} \times \vec{\phi}_i + \vec{\phi}_i \cdot \vec{\nabla} \times \vec{\phi}_j) \rangle_V \\ & + \langle K_{23}\, (\vec{n} \cdot \vec{\nabla} \times \vec{\phi}_i + \vec{\phi}_i \cdot \vec{\nabla} \times \vec{n})(\vec{n} \cdot \vec{\nabla} \times \vec{\phi}_j + \vec{\phi}_j \cdot \vec{\nabla} \times \vec{n}) \rangle_V + \langle K_{34}\, (\vec{\nabla} \times \vec{\phi}_i) \cdot (\vec{\nabla} \times \vec{\phi}_j) \rangle_V \\ & + \langle K_4\, (\vec{\vec{\nabla}} \vec{\phi}_i) : (\vec{\vec{\nabla}} \vec{\phi}_j) \rangle_V - \langle \epsilon_0 \epsilon_a\, (\vec{E} \cdot \vec{\phi}_i)(\vec{E} \cdot \vec{\phi}_j) \rangle_V + \langle \gamma''(\vec{n} \cdot \vec{v})\, (\vec{\phi}_i \cdot \vec{v})(\vec{\phi}_j \cdot \vec{v}) \rangle_S + \langle \lambda\, \vec{\phi}_i \cdot \vec{\phi}_j \rangle_V, \end{aligned} \tag{30}$$

where λ is the interpolating function associated with $\boldsymbol{\Lambda}_{(k)}$.

There are two main assumptions in the TCG algorithm: the Hessian must be symmetric (but not necessarily positive and definite), and the preconditioner must be symmetric positive definite (SPD). Although the first hypothesis is always verified, we empirically noticed that far from the minimum, the AMG preconditioner is not necessarily SPD, which is very often linked with an artificial convergence in only one step. For this reason, we recompute the descent direction with the unpreconditioned TCG algorithm when the preconditioned TCG algorithm has converged in only one step. With this empirical criterion, the computed solution always verifies the descent condition given in Eq. (24) and the inequality $m_k(\boldsymbol{\delta N}_{\perp}) \leqslant m_k(\boldsymbol{0})$.

Once the descent direction $\boldsymbol{\delta N}$ is computed from the TCG algorithm, one needs to check *a posteriori* the validity of the quadratic model m_k. First, we compute the updated value of the solution $\mathcal{P}(\boldsymbol{N}_{(k)} + \boldsymbol{\delta N})$, where $\mathcal{P}$ represents the operation of normalisation of each local director value $\vec{n}_i \to \vec{n}_i / |\vec{n}_i|$. Second, we compute the trust ratio ρ_k, defined as the ratio

between the actual and predicted energy reduction:

$$\rho_k = \frac{f[\mathcal{P}(\boldsymbol{N}_{(k)} + \boldsymbol{\delta N})] - f(\boldsymbol{N}_{(k)})}{m_k(\boldsymbol{\delta N}_\perp) - m_k(\boldsymbol{0})}. \tag{31}$$

Last, we apply the following update rules:

$$\boldsymbol{N}_{(k+1)} = \begin{cases} \mathcal{P}(\boldsymbol{N}_{(k)} + \boldsymbol{\delta N}) & \text{if } \rho_k > 0 \\ \boldsymbol{N}_{(k)} & \text{if } \rho_k \leqslant 0 \end{cases}, \tag{32}$$

$$\Delta_{k+1} = \begin{cases} \gamma_2\, \Delta_k & \text{if } \rho_k > \eta_2 \\ \Delta_k & \text{if } \rho_k \in]\eta_1, \eta_2] \\ \gamma_1\, \Delta_k & \text{if } \rho_k \leqslant \eta_1 \end{cases}, \tag{33}$$

with $0 < \eta_1 \leqslant \eta_2 < 1$ and $0 < \gamma_1 < 1 < \gamma_2$. Equation (32) implies that we keep the step only if the energy has decreased, and Eq. (33) allows us to dynamically update the trust radius. In particular, the trust radius is always decreased if the trust ratio is too small (in which case, we do not trust our quadratic model).

We can now present a formal statement of our algorithm:

(1) **Initialization:** Choose $\boldsymbol{N}_{(0)}$ verifying $\boldsymbol{C}(\boldsymbol{N}_{(0)}) = 0$, and parameters Δ_0, $\eta_{1,2}$, and $\gamma_{1,2}$. Set $k = 0$.

(2) **Assembling:**

(i) Compute $\boldsymbol{B}_{(k)}$, $[\boldsymbol{B}_{(k)}^\intercal\, \boldsymbol{B}_{(k)}]^{-1}$ and $\boldsymbol{G}_{(k)}$ using Eqs. (21), (22), and (23).

(ii) Compute the Lagrange multiplier $\boldsymbol{\Lambda}_{(k)}$ with Eq. (20).

(iii) Compute the Hessian $\boldsymbol{A}_{(k)}$ with Eq. (30).

(iv) Compute the null space matrix $\boldsymbol{Z}_{(k)}$ with Eq. (26).

(v) Compute the reduced gradient $\boldsymbol{G}_{\perp(k)}$ and Hessian $\boldsymbol{A}_{\perp(k)}$ with Eqs. (27) and (28).

(3) **Solving:**

(i) Find the vector $\boldsymbol{\delta N}_\perp$ which approximately solve Eq. (29) with the preconditioned TCG algorithm.

(ii) If the TCG algorithm has converged in only one step, restart the TCG algorithm without preconditioner.

(iii) Compute the solution update: $\boldsymbol{\delta N} = \boldsymbol{Z}_{(k)}\, \boldsymbol{\delta N}_\perp$.

(4) **Update:**

(i) Compute $\mathcal{P}(\boldsymbol{N}_{(k)} + \boldsymbol{\delta N})$ and ρ_k with Eq. (31).

(ii) Compute $\boldsymbol{N}_{(k+1)}$ and Δ_{k+1} with Eqs. (32) and (33).

(iii) If $\rho_k > 0$ and $|f(\boldsymbol{N}_{(k+1)}) - f(\boldsymbol{N}_{(k)})| < 10^{-16}$, stop, else set $k = k + 1$ and go to step 2.

In this algorithm, the stopping criterion is based on the energy variation between two consecutive steps, but a stopping criterion based on the residual [i.e., the norm of the first-order optimality condition in Eq. (17)] is also valid. On a practical note, our algorithm was implemented in C++, and the finite element library Deal.II [17] was used to assemble the matrices and vectors.

Note that our algorithm can theoretically converge to a saddle point if it never encounters a direction $\boldsymbol{\delta N}$ along which the curvature $\boldsymbol{\delta N}^\intercal\, \boldsymbol{A}_{(k)}\, \boldsymbol{\delta N}$ is negative. To ensure that the computed texture corresponds to a minimum of the free energy, we need to check the validity of Eq. (19) at the end of our algorithm: the final reduced Hessian must be SPD. This can be efficiently checked by using the fact that the Cholesky decomposition of a matrix exists if and only if this matrix is SPD [18]. Using the library CHOLMOD, we successfully computed the Cholesky decomposition of the final reduced Hessian for all the computed textures. This shows that all these textures indeed correspond to a minima of the free energy.

In the following, we give two examples of application of our numerical code.

III. MEASUREMENT OF THE ANCHORING ENERGY AT THE CHOLESTERIC-ISOTROPIC INTERFACE OF TWISTED BIPOLAR DROPLETS

In this section, we use our algorithm to measure the anchoring energy at the cholesteric-isotropic (ChI) interface when the anchoring is planar. In this case, the cholesteric droplets often contain two diametrically opposed point defects [bipolar structure, Fig. 1(a)]. Here we show experimentally and numerically that for a LC of negative dielectric anisotropy, it is possible, by applying a high electric field, to stretch these point defects into surface disclination lines [Fig. 1(b)]. These defects have a minimal energy when there is no twist inside the droplet, whereas the bulk energy is minimal when the twist is equal to the equilibrium twist. This energetic competition leads to a partially unwound helix in the direction of the electric field that is detectable optically. As this effect strongly depends on the ratio R/l_a of the droplet radius R over the anchoring extrapolation length $l_a = K_1/W_a$, it can be used to measure l_a. We emphasize that all the surface defects we are speaking about in this paper are virtual, which means that their singular

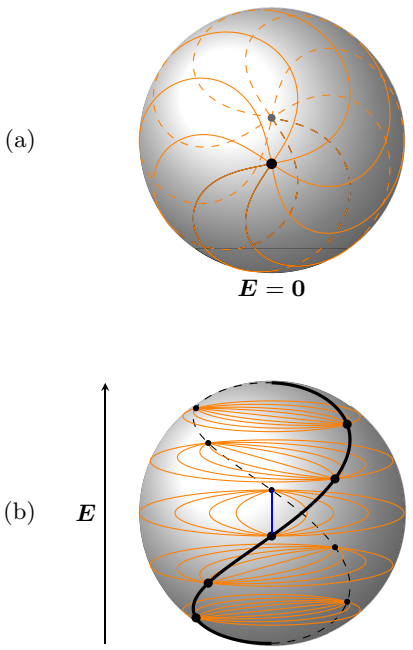

FIG. 1. Two configurations of a cholesteric droplet when the anchoring is planar at the surface and the LC is of negative dielectric anisotropy. In panel (a), there is no electric field and the droplet adopts a bipolar structure with two virtual point defects diametrically opposed (defining the polar axis). Only the director field lines on the surface of the droplet are represented (orange lines). In panel (b), an electric field E is applied vertically. In this case, the two point defects are stretched into two virtual surface disclination lines (thick solid and dashed lines). The director field lines are the orange solid lines. By convention, we will call "polar axis" the axis drawn in blue solid line that joins the two disclination lines in the equatorial plane. For the sake of simplicity, the configuration represented here corresponds to the limit $W_a \to \infty$ and $E \to \infty$.

core is out of the droplets, in the isotropic liquid. For this reason, these point (line) defects correspond to localized disk (ribbon)-shaped regions on the surface, where the anchoring conditions are not satisfied and the anchoring energy is very high.

A. Experimental procedure

To detect the helix distortion induced by the electric field inside the droplets, we measured their optical transmission between crossed polarizer and analyzer as a function of their orientation with respect to the polarizer, when their "polar axis" (defined in the caption of Fig. 1) is parallel to the glass plates. This orientation is forced by the electric field since the LC is of negative dielectric anisotropy. If the temperature is homogeneous, the droplets are fixed and this measurement can only be performed by rotating either the sample or the analyzer and the polarizer simultaneously, which is not convenient. For this reason, we simplified the measurement by taking advantage of the Lehmann effect [19,21,22]. Indeed, it was known for a long time that the internal texture of cholesteric droplets slowly rotates when the droplets are subjected to a small temperature gradient G. We used this effect to directly measure the optical transmission as a function of time by assuming that the texture of the droplets remains the same as at equilibrium during the rotation. Knowing the period of rotation, we then deduced the optical transmission as a function of the angle between the "polar axis" and the polarizer.

In practice, we used the same two-ovens experimental setup and the same procedure as in Ref. [22] to observe the Lehmann effect. In brief, each sample is constituted of two glass plates separated by nickel wires of calibrated diameter. The plates are covered by two layers: an ITO layer, which allows us to orient the cholesteric droplets with a 10 kHz vertical electric field of $0.75\,\mathrm{V}/\mu\mathrm{m}$, and a 20-nm-thin polymercaptan layer, which ensures a planar sliding anchoring and a good dewetting of the cholesteric phase on the plates. Note that the ITO layer was removed in the vicinity of the nickel wires to avoid a short-circuit, and that heating effect due to the ITO layer remains moderate at 10 kHz [23] and can be corrected by slightly decreasing the mean temperature of the sample. The sample thickness h was measured with a spectrometer to within $\pm 0.1\ \mu$m before each experiment. Each sample was filled with the liquid crystal CCN-37 (4α,$4'\,\alpha$-propylheptyl-1α,$1'\,\alpha$-bicyclohexyl-4β-carbonitriles from Nematel, Germany) doped with a mass fraction $C = 0.527$ wt.% of the chiral molecule R811 (R-[+]-octan-2-yl 4-[{4-(hexyloxy)benzoyl}oxy] benzoate from Merck, Germany). This mixture was already characterized by Oswald *et al.* [19]. The values of the main physical constants used in our calculations are given at the transition temperature T_{ChI} in Table I. Once filled, each sample was sandwiched between two ovens regulated to within $\pm 1/100\,^{\circ}$C. Two very thin layers of glycerol ensured a good thermal contact between the sample and the ovens. In these conditions, the sample is subjected to a temperature gradient G proportional to the difference of temperature $\Delta T = T_+ - T_-$ between the two ovens. Droplets are nucleated near the cold plate by setting the mean temperature of the sample $\bar{T} = (T_+ + T_-)/2$ to be between temperature T_{sol}, at which the cholesteric phase starts melting, and temperature T_{liq}, at which the sample is completely isotropic. We estimated that the freezing range is typically $T_{\mathrm{liq}} - T_{\mathrm{sol}} \approx 0.1^{\circ}$C. The radii of the droplets can be changed by adjusting $\bar{T}$ while keeping ΔT constant.

TABLE I. Values at the transition temperature of the main physical constants of the mixture CCN-37+0.527 wt.% R811 [19]. Note that the value of K_4 was estimated with the theoretical relation $K_4 = (K_1 + K_2)/2$. This formula was first obtained by Nehring and Saupe (with a different convention for the definition of the K_i) from a molecular Cauchy-like approach [20].

Constants	Values at T_{ChI}
K_1 (pN)	0.96
K_2 (pN)	0.84
K_3 (pN)	1.37
K_4 (pN)	0.90
q ($\mu\mathrm{m}^{-1}$)	0.308
ϵ_a	−2.34
Δn	0.016

We now return to the measurement of the optical transmittance. Because of the spatial variations of the optical index inside the droplets, light rays can deviate inside and refract at their surface. To avoid these complications, we measured the optical transmission only at the center of the droplets by focalizing a Gaussian beam of wavelength $\lambda = 488\,\mu$m coming from a solid state laser (Sapphire SF 488-100 CW CDRH, Coherent). In this case, the rays propagate in a straight line and the optical calculations are much simpler. In practice, the laser beam was first filtered (output power of $0.1\,\mu$W), then cleaned by a spatial filter and focused onto the sample thanks to a condenser lens (focal length 1 cm). Last, the focus point of the beam (waist w of $1.5\,\mu$m) was centered on the droplet chosen with the help of an XY translation stage, and the intensity signal at the center of the beam was measured as a function of time.

To sum up, we show in Fig. 2 a schematic of the entire setup, constituted of three parts:

—the middle part, formed by the two ovens and the sample;

—the upper part designed to visualize the sample. It includes a SCMOS camera (Zyla 4.2 PLUS, Andor) collecting the intensity signal though a microscope objective ($\times 10$);

—the lower part designed to illuminate the sample either with a uniform lighting or with the laser beam, thanks to a beam splitter.

Note that the uniform lighting coming from the TL lamp was used to observe the droplets and center the laser beam on the droplet chosen but was always switched off during the acquisition. Finally, the transmission T at the center of the droplets was calculated from formula

$$T = \frac{I - I_{\perp}}{I_{\parallel} - I_{\perp}}, \tag{34}$$

where $I_{\perp}(I_{\parallel})$ is the raw intensity measured by our camera in the isotropic liquid between perpendicular (parallel) polarizer and analyzer and I the raw intensity measured at the center of the droplets between perpendicular polarizer and analyzer.

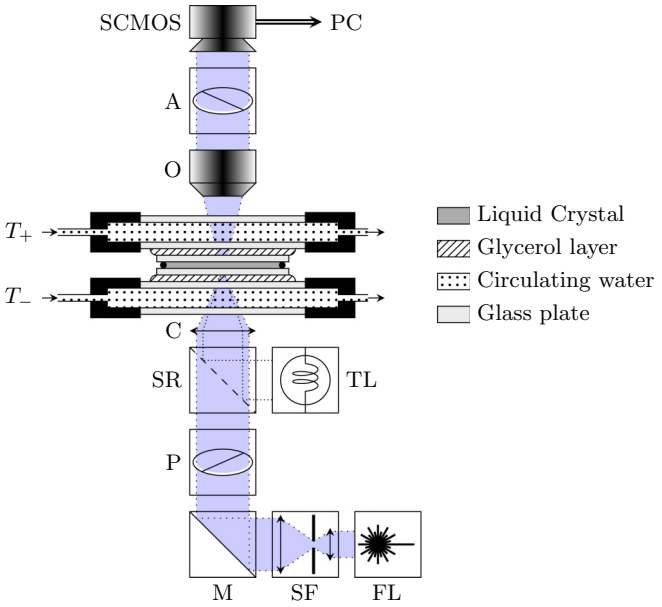

FIG. 2. The setup used to measure the transmission of the droplets. Observations were made with a SCMOS camera through the objective (O). Thanks to the beam splitter (SR), the sample was illuminated either globally with the lamp (TL) or locally by focusing with the condenser (C) the Gaussian beam of the laser (FL) cleaned by the spatial filter (SF). The orientations of the polarizer (P) and the analyzer (A) can be set independently. At last, the ovens and the sample can be moved horizontally with an XY translation stage.

B. Numerical procedure

Using the algorithm described in Sec. II, we computed the textures of oriented cholesteric droplets by taking the values of the parameters given in Table I. There remain two free parameters, namely the anchoring strength W_a and the radius R of the droplet, whose shape was assumed to be spherical. The droplet was partitioned with the default spherical mesh of the library Deal.II, whose characteristics are recalled in Table II.

We also assumed that the electric field was not perturbed by the variation of the dielectric constant inside the droplet, and set $E = 0.75\,\mathrm{V}/\mu\mathrm{m}$. We verified *a posteriori* this hypothesis by solving with Mathematica the Maxwell equations inside the sample for a completely oriented droplet. In this case, the effective dielectric constant inside the droplet is $\epsilon_\perp$ and the dielectric constant outside the droplet is $\epsilon_I \approx (2\epsilon_\perp + \epsilon_\parallel)/3$. When the droplet radius is between 5 and 15 μm, we found that the value of the electric field inside the droplet was modified by less than 2%. In addition, the direction of the electric field was only perturbed outside the droplet.

TABLE II. Characteristics of the spherical mesh. c is the refinement cycle, M_c is the associated number of vertices, and d_c is the maximal cell diameter renormalized by the droplet radius.

c	M_c	d_c
1	79	1.2248
2	517	0.6124
3	3 817	0.3062
4	29 521	0.1531
5	232 609	0.0765
6	1 847 617	0.0383

Note that in our numerical code, the free energy was rescaled by the typical energy $F_0 = K_1\,R$ and that all lengths were rescaled by the droplet radius R. This allowed us to always work with a sphere of radius unity. A typical computation job works as follows. First, a trial value of the anchoring energy was set. Then, we minimized the free energy of the smallest droplet with a Nested Iteration algorithm: for each refinement cycle (except the last), the minimization was followed by a mesh refinement step, and the output solution on the coarser mesh was used as input on the finer mesh. This method optimized the convergence time toward the finest solution. Note that due to memory limitations, we were not able to go beyond the sixth cycle. Finally, we used a ramp algorithm to compute the textures for different radii: for each radius (except the last one), the minimization was followed by a small update of the radius, and the output solution of the previous step was used as input for the new step.

We repeated this computation pattern for different anchoring energies and calculated each time the transmission signal under crossed polarizers with the method of Jones matrix. We found that this signal can always be modelized by a shifted and rescaled cosine when plotted as a function of the droplet orientation. For this reason, we chose to keep only the maximum and the minimum of the transmission, to allow an easy comparison with the experimental data. The final output of our computation is therefore the minimum and the maximum of the transmission at the center of the droplet as a function of the radius and the anchoring length: $T_{\min}(R,l_a)$ and $T_{\max}(R,l_a)$.

C. Results and discussion

We now discuss our experimental and numerical results. First, we tested the influence of the temperature gradient on the shape of the oriented droplets. We measured the minimum $T_{\min}$ and the maximum $T_{\max}$ of the transmission for $\Delta T = 0.5\,^\circ\mathrm{C}, 1\,^\circ\mathrm{C}$, and $2\,^\circ\mathrm{C}$ (equivalent to $G = 0.9\,\mathrm{mK}/\mu\mathrm{m}$, $1.8\,\mathrm{mK}/\mu\mathrm{m}$, and $3.6\,\mathrm{mK}/\mu\mathrm{m}$). The values of $T_{\min}$ and $T_{\max}$ are plotted as a function of the droplet radius in Fig. 3. A first observation is that all the points collapse on the same master curve, independently of the temperature gradient. This observation shows that the shape of the droplet is independent of G. A second observation is that there is a discontinuity in the slope when the droplet diameter is equal to the sample thickness $h \approx 41.49\,\mu$m measured with our spectrometer. This slope change can be interpreted as the critical size for which the droplets become confined and touch the two plates. This observation shows that the droplets are spherical at this point since their thickness is equal to their diameter. This result suggests that, in our experiments, the droplets are spherical as long as their diameter is smaller than the thickness. This result may be surprising because the droplets are subjected to an electric field. Indeed, Auernhammer *et al.* showed that LC droplets submitted to an AC field can be deformed, due to surface charges interacting with the electric field. The amplitude of deformation is expected to be proportional to the square of the electric field, with a proportionality constant highly dependent on the frequency of the AC field: the higher the frequency,

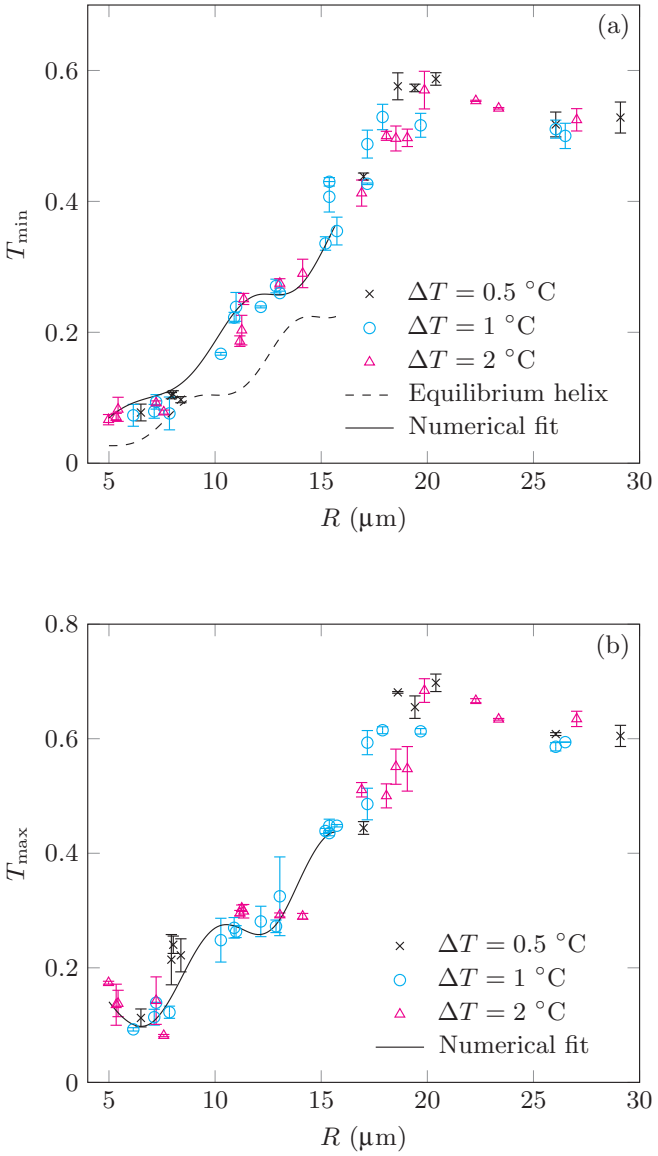

FIG. 3. Minimum (a) and maximum (b) of the transmission signal as a function of the droplet radius. Crosses are experimental points and dashed and solid lines are numerical curves.

the weaker the deformation. This is why we chose a 10 kHz frequency for the electric field. To test the relevance of the deformation effect, we reproduced similar measurements with a lower field intensity of 0.5 V/μm. We found again a slope change at $2R \approx h$ and saw no visible variation of the droplet radius when switching back and forth between the two field intensities. This result shows that we can neglect the deformation effect when the 10 kHz electric field intensity is lower than 0.75 V/μm and the droplet radius is smaller than 20 μm ($\sim h/2$). This study confirms that the droplet shape is spherical, as it must be at equilibrium without electric field and temperature gradient. This observation is also in agreement with the findings of Yamamoto *et al.* [24], who showed by using fluorescence confocal polarizing microscopy that the droplets remain spherical, even when they are in a temperature gradient.

Next, we numerically computed the curves $T_{\min}(R,l_a)$ and $T_{\max}(R,l_a)$ with $R = 5$ to 16 μm and $l_a = 0.6$ to 1.1 μm. Note here that we were not able to simulate droplets of radius larger than 16 μm with a good enough accuracy because, in this case, the surface disclination lines are too thin to be resolved. Indeed, we noticed that the thickness of the disclination lines is typically 1.6 μm. For a droplet of 16 μm, this means that the dimensionless thickness of the line on the unit sphere is equal to 0.1. This value must be compared with the typical cell diameter of 0.04 on the sixth level of refinement, which is not small enough to get reliable results. For the smaller droplets, the relative error ϵ on $T_{\min}$ and $T_{\max}$, defined as

$$\epsilon = \max\left(\left|\frac{T_{\min}^{(6)} - T_{\min}^{(5)}}{T_{\min}^{(6)}}\right|, \left|\frac{T_{\max}^{(6)} - T_{\max}^{(5)}}{T_{\max}^{(6)}}\right|\right),$$

was always less than 5%. In this equation, $T^{(k)}$ is the transmittance computed on the kth refinement cycle. This formula can be interpreted as an upper bound for the true error if the convergence is at least linear, which is always the case in our simulations.

As the value of K_4 in Table I was obtained from a theoretical model and not from an experimental measurement, we wondered whether a different value of K_4 could significantly change $T_{\min}$ and $T_{\max}$. For this reason, we recomputed the transmission curves for values of K_4 ranging from 0.48 to 1.68 pN [the upper bound allowed by the Ericksen inequalities given in Eq. (5)], and found that the relative variation of the transmission was always less than 5%. This result shows that we can neglect here the role of the elastic constant K_4.

Finally, we fitted our experimental data with the numerical curves $T_{\min}(R,l_a)$ and $T_{\max}(R,l_a)$. Cubic spline interpolation was used to extend the discrete numerical data, and the least-square solution was computed with the Levenberg-Marquardt algorithm. We plotted in Fig. 3 the least-square curves $T_{\min}(R,l_a^*)$ and $T_{\max}(R,l_a^*)$ (solid lines) by taking the fitted value of the anchoring extrapolation length with 95% confidence bounds: $l_a^* = 0.82 \pm 0.07$ μm. For comparison, we also plotted the theoretical signal $T_{\min}$ calculated with a droplet in which the equilibrium helix is not deformed. As we can see, this curve shifts much more from the experimental data than the numerical curves $T_{\min}(R,l_a^*)$ and $T_{\max}(R,l_a^*)$. This validates the relevance of our numerical approach. Note that the usual method of measurement of l_a proposed by Faetti [25] and Yokoyama [26] cannot be applied with the CCN-37, contrary to the method presented here. Indeed, this LC has negative dielectric and magnetic anisotropies, which makes impossible the destabilization of the director orientation out of the plane of the N-I interface by application of a vertical or horizontal field. This is obvious when the field is vertical, whereas a horizontal field will only twist the director field because $K_2 < K_{1,3}$, without changing its orientation with respect to the normal to the interface.

To go further in the comparison between our numerical model and the experiments, we used the Jones matrix method to compute the image between crossed polarizer and analyzer of a typical droplet for two different orientations of the polar axis with respect to the polarizer. The result is shown in Fig. 4 for a droplet of radius 9 μm. In this figure, the left images are experimental and the right ones have been numerically calculated. The experimental images were taken in green light (546 nm) by replacing the condenser lens C with a Köhler

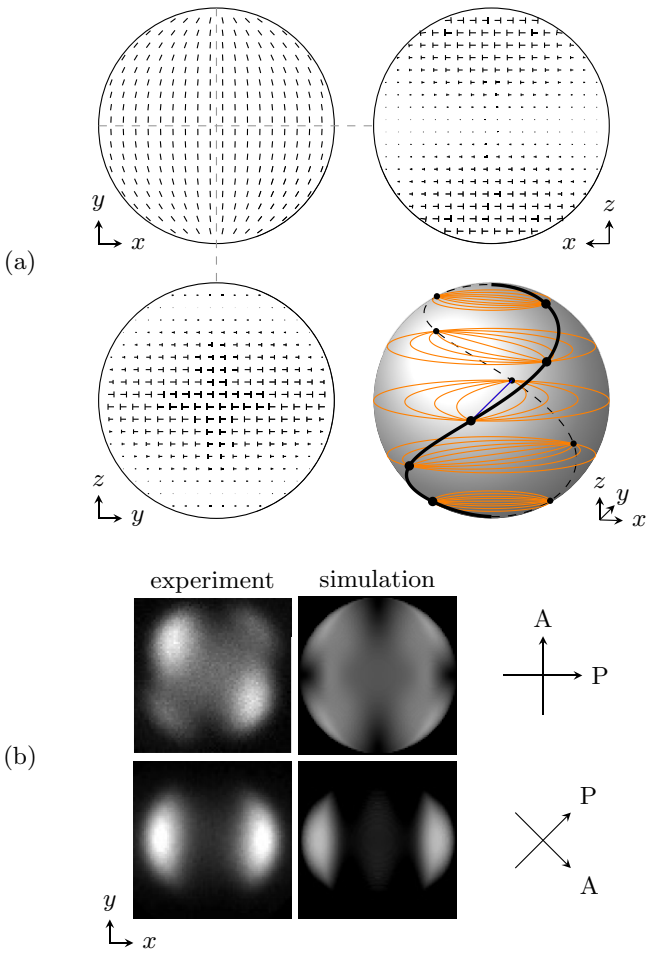

FIG. 4. (a) Three cuts of the director field for $R = 9\,\mu$m along the xy,xz and yz planes. The orientation of the droplet with respect to the three axes is given in the bottom right corner. Tilted molecules are represented by nails, proportional in length to the director projection in the plane of the drawing. The nail point is oriented towards the reader. (b) Numerical and experimental images of the same droplet than in (a). In all these images, the polar axis (as defined in Fig. 1) is vertical and aligned with the y-axis.

illumination setup. The aperture diaphragm was closed as much as possible to work in parallel light. The numerical images were calculated by neglecting the ray deviations. As we can see, the agreement between the numerics and the experiment is rather good, but not perfect, in particular when the droplet polar axis is parallel to the polarizer. This could be due to the deviations of the light rays inside the droplet, especially near the surface disclination lines, which are neglected in the optical calculations. Taking into account these effects is difficult and out of the scope of this paper.

IV. STABILITY ANALYSIS OF BANDED AND DOUBLE TWIST DROPLETS

In most of the LCs, the anchoring is tilted at the cholesteric-isotropic interface. With these materials, two types of droplets are usually observed in the coexistence region with the isotropic liquid [6,7]. The first ones have a revolution axis and present a double twist structure inside as shown recently

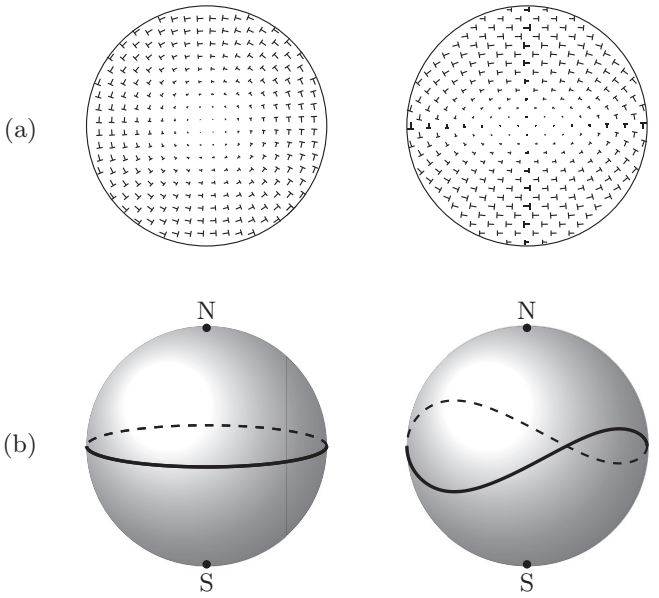

FIG. 5. (a) Equatorial cut of the director field in the DT case (left) and ST case (right). (b) Topology of the surface virtual defects (black dots) and disclination lines (black lines) in a DT droplet (left) and ST droplet (right).

by Yoshioka *et al.* [6]. The second ones are mainly twisted in a single direction and present a banded texture under the microscope. Contrary to the previous ones, these droplets are only invariant under a π-rotation along an axis perpendicular to the main twist axis. The director field inside these two types of droplets is shown in Fig. 5(a). These droplets have also a virtual disclination lines on their surface shown in Fig. 5(b). For the double twist (DT) droplets (left drawing), this line is along the equator and perpendicular to the NS revolution axis (C_∞ axis). For the single twist (ST) droplets (right drawing), this line deforms around the equator and the NS axis becomes a C_2 axis. Experimentally, the passage from DT to ST droplets depends on the size of the droplets [6,7]: the small droplets are of DT type whereas the big ones are of the ST type. This structural transition during which the symmetry of revolution is broken was recently studied by Yoshioka *et al.* [6] both experimentally and theoretically. In this work, the dominant role of the saddle-splay constant was recognized and a method of measurement of K_4 was proposed, based on an analysis of the optical properties of the DT droplets. On the other hand, this model used a very simple ansatz for the director field inside the DT droplets and completely neglected the role of the anchoring energy. Our goal in this section is to test to which extend these assumptions are justified by comparing the results of this simplified model with numerical simulations. The comparison will be made for the material 7CB (heptylcyanobiphenyl) for which the elastic constants, the anchoring angle, and the anchoring energy are well known [25,27].

A. Numerical procedure

The numerical procedure to compute the textures of the cholesteric droplets is very similar to that described in the previous section. The calculations were performed for the LC

TABLE III. Values at the transition temperature of the main physical constants of the mixture 7CB+R811 [25,27].

Constants	Values at T_{ChI}
K_1 (pN)	2.2
K_2 (pN)	1.2
K_3 (pN)	2.0
$l_a = K_1/W_a$ (μm)	2.65
θ_a (deg)	52.6

7CB (heptylcyanobiphenyl) for which the elastic constants $K_i (i = 1-3)$ and the surface properties are known (Table III). Note that we did not measure the anchoring length by using the method presented in the previous section, because the 7CB is of positive dielectric anisotropy, and therefore cannot be oriented as in the case of the CCN-37.

In our calculations, we assumed that these constants do not change when a small amount of chiral molecules (such as R811, for instance) is added and we took as adjustable parameters the equilibrium twist q (proportional to the concentration of chiral dopant), the radius R of the droplets and the Gauss elastic constant K_4. The same spherical mesh as before was used to partition the droplet.

At the start of each computation job, we chose the values of two dimensionless numbers ql_a and K_4/K_1. In this way, the cholesteric phase was completely characterized. To calculate the texture of the droplets as a function of their radius, we used as in the previous section a refinement phase followed by a ramp phase, starting this time from the biggest droplet. For each radius R, we also computed the dimensionless energy $\tilde{F}(qR, ql_a, K_4/K_1)$ of the droplet and the quantity:

$$\psi\left(qR, ql_a, \frac{K_4}{K_1}\right) = \frac{1}{V}\int_V dV \left[\frac{D\vec{n}}{D\Theta}\right]^2, \qquad (35)$$

where $D\vec{n}/D\Theta = \vec{e}_z \times \vec{n} - \partial\vec{n}/\partial\theta$ is the variation rate associated with a solid rotation around the polar axis $\vec{e}_z$ defined in Fig. 5 [28]. This quantity can be used as an order parameter to characterize the symmetry breaking during the transition between ST and DT droplets. Indeed, $\psi = 0$ in the DT droplets since $D\vec{n}/D\Theta = 0$, the polar axis $\vec{e}_z$ being a C^∞ axis. Conversely, $\psi \neq 0$ in a ST droplet because the polar axis is no longer a C^∞ axis. Finally, the critical radius R_c between the two regimes was deduced from the plot of the function $\psi(qR)$.

Note that we only kept the results for which the relative error on ψ, defined as in the last section, was less than 10%. The discarded results essentially concerned the droplets calculated in the very strong anchoring regime when $ql_a \leqslant 0.4$: in this regime, the surface disclination was too thin to be well approximated, even on the finest mesh of the sixth refinement cycle.

B. Results and discussion

We now discuss our numerical results. First, we determined the order of the transition between ST and DT droplets for a particular value of the Gauss constant $K_4/K_1 = 0.78$ (this value was calculated from the theoretical relation of Nehring and Saupe: $K_4 = (K_1 + K_2)/2$ [20]). We plotted in Fig. 6 the value of ψ as a function of qR for different values of the dimensionless anchoring length ql_a. Three observations can be made:

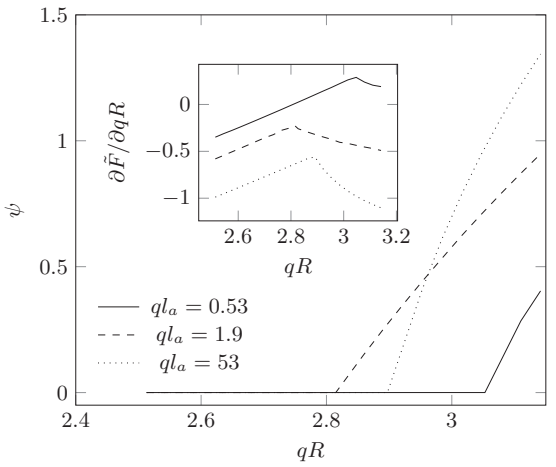

FIG. 6. Value of the order parameter ψ as a function of the dimensionless radius qR for three values of the dimensionless anchoring length ql_a. Inset: First-order derivative of the dimensionless energy as a function of the dimensionless radius. The break in the slope is the hallmark of a second-order transition. All these curves were computed by taking $K_4/K_1 = 0.78$.

(1) the order parameter is equal to zero for the small droplets and different from zero for the big droplets, which shows that DT droplets are stable only for the small radii;

(2) the critical radius R_c for which the transition occurs depends on the dimensionless anchoring length ql_a;

(3) the order parameter ψ is continuous at the transition, with a slope discontinuity at this point.

This last observation suggests that the transition is of the second order. To confirm this point, we plotted in the inset of Fig. 6 the derivative of the rescaled energy $\partial\tilde{F}/\partial qR$ as a function of qR. As we can see, there is a break in the slope of the curve at the transition. This shows that the second derivative $\partial^2\tilde{F}/\partial(qR)^2$ is discontinuous at the transition, which is the mark of a second-order transition. In addition, we found that the order of the transition remained the same for all the tested values of ql_a and K_4/K_1. In the following, the critical radius R_c was always determined from the break in the slope of the curve $\psi(qR)$.

Next, we explored the dependence of the critical radius R_c on ql_a and K_4/K_1. The effect of the rescaled Gauss constant K_4/K_1, calculated both from our numerical code and the Yoshioka *et al.* model [6], is shown in Fig. 7(a). In all the cases, the transition completely disappears when $K_4/K_1 = 0$ (the lower bound allowed by the Ericksen inequalities given in Eq. (5)). In this limit, the DT droplets are no longer stable, even at very small radius.

We also plotted in Fig. 7(b) the dimensionless critical radius qR_c as a function of the dimensionless anchoring length ql_a. This graph shows that the anchoring energy plays a non-negligible role—contrary to what is assumed in the Yoshioka *et al.* model—as long as $ql_a < 10$, which is the case in most experiments. Moreover, this effect is not trivial when

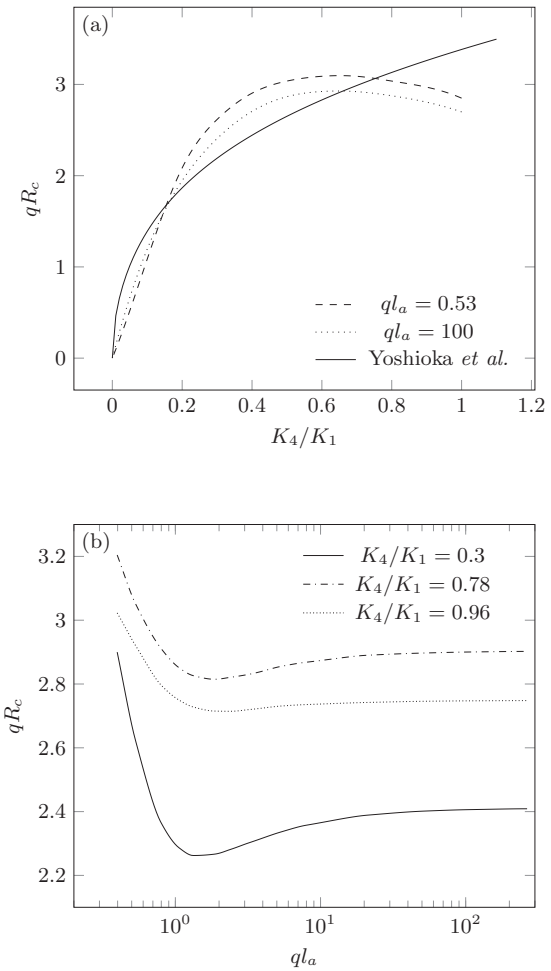

FIG. 7. (a) Dimensionless critical radius qR_c as a function of the ratio K_4/K_1 for two values of the dimensionless anchoring length ql_a (dashed and dotted lines). The solid line was calculated from the Yoshioka *et al.* model. (b) Same quantity as a function of ql_a for three values of the ratio K_4/K_1.

ql_a decreases since the critical radius R_c starts to decrease in the intermediate anchoring regime ($1 \leqslant ql_a \leqslant 10$) before increasing in the strong anchoring regime ($ql_a \leqslant 1$).

Finally, we compared the numerical director field of a DT droplet with the very simple ansatz used in the theoretical model of Yoshioka *et al.* To do this comparison, let us introduce the Euler angles α and β in the local polar frame $(\vec{e}_\theta,\vec{e}_z,\vec{e}_r)$ (cf. Fig. 8). Because $\vec{e}_z$ is along the revolution axis of the droplet, α and β do not depend on the polar angle θ and the director field reads

$$\vec{n}(r,z) = \cos\beta(r,z)\vec{e}_r - \sin\beta(r,z)\sin\alpha(r,z)\vec{e}_\theta + \sin\beta(r,z)\cos\alpha(r,z)\vec{e}_z.$$

To simplify their calculations, Yoshioka *et al.* assumed a very simple form for these angles:

$$\alpha(r,z) = q_e r, \qquad \beta(r,z) = \pi/2, \tag{36}$$

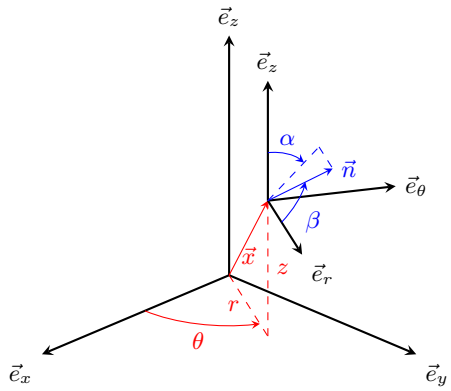

FIG. 8. Coordinate and angle conventions for the director field inside a DT droplet. The position is parametrized by the polar coordinates (r,θ,z) by taking the z axis along the revolution axis of the droplet. The director field is parametrized by the Euler angles (α,β) defined in the local frame $(\vec{e}_\theta,\vec{e}_z\vec{e}_r)$.

where q_e is an effective twist which depends on qR and the elastic constants K_i and must be calculated by minimizing the total energy of the droplet.

To test the validity of this ansatz, we computed the director field of a DT droplet by taking $ql_a = 100$ (which corresponds to the weak anchoring regime, as in the model of Yoshioka *et al.*), $qR = 2.7$ ($\leqslant qR_c$) and $K_4/K_1 = 0.78$ (theoretical value of Nehring and Saupe [20]). The associated Euler angles α and β are plotted on Fig. 9 as a function of r/R for different z. A first observation is that the tilt angle β of the director with respect to $\vec{e}_r$ deviates from $\pi/2$ as soon as $z \neq 0$, in contrast with Yoshioka *et al.* model. A second observation is that the twist angle α is not linear in r (again in disagreement with Yoshioka *et al.* model), although it seems roughly independent of z. More awkward, the theoretical director field obtained from Yoshioka *et al.* model gives a profile $\alpha_{\text{th}}(r,z) = q_e r$ (black line in Fig. 9) very different from the numerical one. In particular, the slope q_e of this theoretical profile is 30% smaller than the mean slope of our numerical profile $\alpha(r)$.

This disagreement between the ansatz Eq. (36) and the real director field is problematic, because it clearly shows that the Yoshioka *et al.* measurement method of K_4 is biased. Indeed, this method relies on fitting the experimental average twist q_e (measured from the optical transmission under crossed polarisers) as a function of qR. As the value of q_e obtained from Yoshioka *et al.* model is biased (too small according to our simulations, even in the weak anchoring regime), one could expect that the measured value of K_4 is also biased, especially since this simplified model neglects the anchoring energy.

V. CONCLUSION

In this paper, we presented an algorithm to solve efficiently the equations of the nematoelasticity. This algorithm is based on the renormalized nullspace Newton method of Gartland *et al.*, with three important modifications: an arbitrary unstructured grid is allowed to discretize the LC domain, a trust-region strategy is used instead of a Newton method, and an algebraic multigrid preconditioner is used to help the convergence. The trust-region strategy allows a very robust convergence

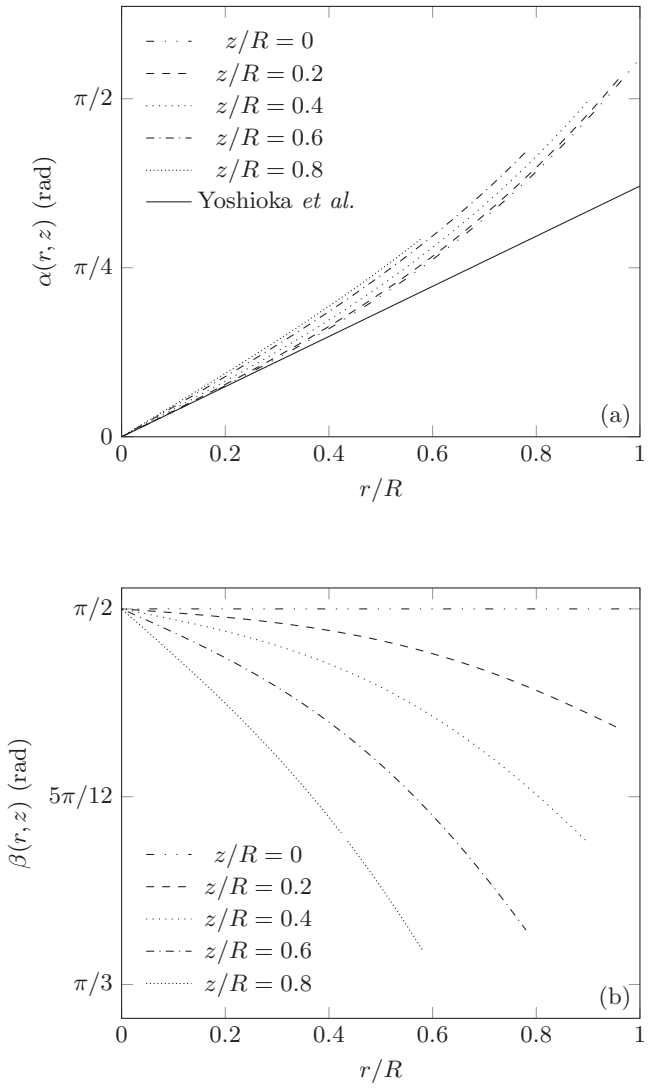

FIG. 9. Euler angles α (a) and β (b) as a function of r/R for different values of z. The director field was computed by taking $ql_a = 100, qR = 2.7$ and $K_4/K_1 = 0.78$.

by automatically interpolating the solution update between the Cauchy direction and the Newton direction. Furthermore, the convergence becomes quadratic near a minimum of the free energy, i.e., the convergence is faster than with a more conventional gradient descent algorithm.

We applied this algorithm to two problems.

The first problem was the measurement of the anchoring length at the ChI interface of a chiral mixture with planar anchoring and negative dielectric anisotropy. By applying a high electric field to the droplets, we obtained a structure whose optical transmission is very sensible to the anchoring length l_a. By measuring and fitting this transmission as a function of the droplet radius, we were able to deduce the value of the anchoring extrapolation length l_a for the studied cholesteric mixture (CCN-37 doped with R811). The value found ($0.87 \pm 0.07\,\mu$m) is 3 to 30 times smaller than the values given by Faetti in cyanobiphenyls [25], which shows that the anchoring is rather strong in CCN-37.

The second problem was the transition between DT and ST droplets in a cholesteric mixture with tilted anchoring. We showed that this transition is of the second order, and disappears when the Gauss constant vanishes ($K_4 = 0$). We compared our results with the analytical model of Yoshioka *et al.*, and found a qualitative (but not quantitative) agreement. In particular, we found that the effect of the anchoring energy cannot be neglected in the moderate and strong anchoring regimes. We also found that, even in the regime of very weak anchoring, the ansatz of Yoshioka *et al.* concerning the director field is rather far from the real solution numerically calculated.

Nevertheless, we believe that Yoshioka *et al.* measurement method of K_4 is promising and could easily be corrected by using the more realistic director fields calculated with our code. More precisely, measuring the optical transmission at the center of DT droplets oriented with their polar axis perpendicular to the observation direction as a function of qR and fitting this curve with our numerical code should give a more exact value of K_4. Such an experiment is planned in the future with a material in which the elastic constants and the surface properties are well known.

Another extension of this work would be to include in our numerical code the Lehmann torque responsible for the rotation of the banded (ST) droplets when they are subjected to a temperature gradient. In this case the experiment shows that there is still a transition between the DT droplets—which do not rotate—and the banded ST droplets—which rotate—above a critical radius R_c that is inversely proportional to $\sqrt{G}$ at large G [7]. This problem could be treated numerically by determining for which radius R_c the static DT solution disappears when G increases. In this case, our code cannot be used directly because the Lehmann torque does not derive from a free energy. On the other hand, the structure could be calculated step by step as a function of G by using an usual relaxation method and by taking as initial solution the one calculated numerically with the current code at $G = 0$.

ACKNOWLEDGMENTS

We thank A. Dequidt for fruitful discussions and Dr. W. Becker from Merck, Germany, for giving us a free sample of R811.

[1] D. Sec, T. Porenta, M. Ravnik, and S. Zumer, Geometrical frustration of chiral ordering in cholesteric droplets, Soft Matter **8**, 11982 (2012).

[2] G. Posnjak, S. Copar, and I. Musevic, Points, skyrmions and torons in chiral nematic droplets, Scientific Reports **6**, 26361 (2016).

[3] F. Xu and P. P. Crooker, Chiral nematic droplets with parallel surface anchoring, Phys. Rev. E **56**, 6853 (1997).

[4] D. Sec, S. Copar, and S. Zumer, Topological zoo of free-standing knots in confined chiral nematic fluids, Nat. Commun. **5**, 3057 (2014).

[5] I. Musevic, Liquid-crystal micro-photonics, Liquid Cryst. Rev. **4**, 1 (2016).
[6] J. Yoshioka, F. Ito, and Y. Tabe, Stability of a double twisted structure in spherical cholesteric droplets, Soft Matter **12**, 2400 (2016).
[7] P. Oswald, Lehmann rotation of cholesteric droplets subjected to a temperature gradient: Role of the concentration of chiral molecules, Eur. Phys. J. E **28**, 377 (2009).
[8] I. Bajc, F. Hecht, and S. Zumer, A mesh adaptivity scheme on the Landaude Gennes functional minimization case in 3D, and its driving efficiency, J. Comput. Phys. **321**, 981 (2016).
[9] L. Gil and J. M. Gilli, Surprising Dynamics of Some Cholesteric Liquid Crystal Patterns, Phys. Rev. Lett. **80**, 5742 (1998).
[10] J. H. Adler, D. B. Emerson, S. P. MacLachlan, and T. A. Manteuffel, Constrained optimization for liquid crystal equilibria, SIAM J. Sci. Comput. **38**, B50 (2016).
[11] E. C. Gartland and A. Ramage, A renormalized newton method for liquid crystal director modeling, SIAM J. Numer. Anal. **53**, 251 (2015).
[12] P. Oswald and P. Pieranski, *Nematic and Cholesteric Liquid Crystals: Concepts and Physical Properties Illustrated by Experiments* (CRC Press, Boca Raton, FL, 2006).
[13] J. L. Ericksen, Inequalities in liquid crystal theory, Phys. Fluids **9**, 1205 (1966).
[14] D. P. Bertsekas, *Nonlinear Programming* (Athena Scientific, Belmont, MA, 1999).
[15] T. Steihaug, The conjugate gradient method and trust regions in large scale optimization, SIAM J. Numer. Anal. **20**, 626 (1983).
[16] M. W. Gee, C. M. Siefert, J. J. Hu, R. S. Tuminaro, and M. G. Sala, ML 5.0 smoothed aggregation user's guide, Tech. Rep. SAND2006-2649 (Sandia National Laboratories, 2006).
[17] W. Bangerth, D. Davydov, T. Heister, L. Heltai, G. Kanschat, M. Kronbichler, M. Maier, B. Turcksin, and D. Wells, The deal. II library, version 8.4, J. Numer. Math. **24**, 135 (2016).
[18] G. H. Golub and C. F. Van Loan, *Matrix Computations*, Vol. 3 (JHU Press, Baltimore, MD, 2012).
[19] P. Oswald, G. Poy, and A. Dequidt, Lehmann rotation of twisted bipolar cholesteric droplets: role of Leslie, Akopyan and Zeldovich thermomechanical coupling terms of nematodynamics, Liq. Cryst. **44**, 969 (2016).
[20] J. Nehring and A. Saupe, On the elastic theory of uniaxial liquid crystals, J. Chem. Phys. **54**, 337 (1971).
[21] O. Lehmann, Structur, System und magnetisches Verhalten flssiger Krystalle und deren Mischbarkeit mit festen, Ann. Phys. **307**, 649 (1900).
[22] P. Oswald and A. Dequidt, Measurement of the Continuous Lehmann Rotation of Cholesteric Droplets Subjected to a Temperature Gradient, Phys. Rev. Lett. **100**, 217802 (2008).
[23] P. Oswald, Elasto- and electro-capillary instabilities of a nematic-isotropic interface: Experimental results, Eur. Phys. J. E **33**, 69 (2010).
[24] T. Yamamoto, M. Kuroda, and M. Sano, Three-dimensional analysis of thermomechanically rotating cholesteric liquid crystal droplets under a temperature gradient, Europhys. Lett. **109**, 46001 (2015).
[25] S. Faetti and V. Palleschi, Nematic-isotropic interface of some members of the homologous series of 4-cyano-4-(n-alkyl) biphenyl liquid crystals, Phys. Rev. A **30**, 3241 (1984).
[26] H. Yokoyama, S. Kobayashi, and H. Kamei, Measurement of director orientation at the nematicisotropic interface using a substrate-nucleated nematic film, Mol. Cryst. Liq. Cryst. **107**, 311 (1984).
[27] N. V. Madhusudana and R. Pratibha, Elasticity and orientational order in some cyanobiphenyls: Part IV. reanalysis of the data, Mol. Cryst. Liq. Cryst. **89**, 249 (1982).
[28] A. Dequidt, G. Poy, and P. Oswald, Generalized drift velocity of a cholesteric texture in a temperature gradient, Soft Matter **12**, 7529 (2016).